

A Material Mask Overlay Strategy for Close to Binary Design-dependent Pressure-loaded Optimized Topologies

Prabhat Kumar*

Department of Mechanical Engineering
Indian Institute of Science, Bengaluru 560012, Karnataka, India

Anupam Saxena

Department of Mechanical Engineering
Indian Institute of Technology Kanpur, Kanpur 208016, Uttar Pradesh, India

Abstract

This paper presents a Material Mask Overlay Strategy topology optimization approach with improved material assignment at the element level for achieving close to black-and-white designs for pressure-loaded problems. Hexagonal elements are employed to parametrize the design domain as this tessellation provides nonsingular local connectivity. Elliptical negative masks are used to find the optimized material layout. The material dilation and material erosion variables of each mask are systematically varied in association with a gray-scale measure constraint to achieve designs close to 0-1. Darcy's law in association with a drainage term is used to formulate the pressure field. The obtained pressure field is converted into the consistent nodal forces using Wachspress shape functions. Sensitivities of the objective and pressure load are evaluated using the adjoint-variable method. The approach is demonstrated by solving various pressure-loaded structures and pressure-actuated compliant mechanisms. Compliance is minimized for loadbearing structures, whereas a multicriteria objective is minimized for mechanism designs.

Keywords: Topology Optimization, Material Masks Overlay Strategy, Design-dependent pressure loads, Honeycomb tessellation, Compliant mechanisms

1 Introduction

Topology optimization (TO) is a numerical technique to find the optimized material layout within a given design domain experiencing external loads with boundary conditions by extremizing the objective subjected to a known set of constraints. External loads can be either constant (design-independent) or variant (design-dependent) with the design evolution during TO. A wide range of applications involving design-dependent pressure loadings can be found, e.g., in aircraft wings and fuselage, ships, wind and snow load experiencing houses, internal and external pressure-loaded pumps and containers, pneumatically and/or hydraulically actuated soft robots [1, 2]. However, treatment of design-dependent loads, e.g., fluidic pressure loads in a TO setting is challenging and involved [2]. This is because, a pressure load alters its magnitude, location and direction as design evolves in TO. The challenges increase further as one seeks optimized, black-and-white designs that are highly appreciated and desirable in TO [3]. The goal here is to present a Material Mask Overlay topology optimization approach with improved material assignment to get pressure-loaded designs close to binary solutions.

The Material Mask Overlay Strategy (MMOS), initially conceived in [4], employs masks to assign material to a group of hexagonal finite elements (FEs) used to parameterize the design domains. Edge-connectivity provided by hexagonal FEs subdued checkerboard patterns/point connections in optimized topologies without additional singularity suppression schemes [5–9]. To our best knowledge however, there is

*Corresponding author: prabhatk@iisc.ac.in

currently no literature available that employs hexagonal FEs for achieving black-and-white pressure-loaded topologies. In a typical two-dimensional TO, a mask is constituted of a non-intersecting, analytical or free-form closed curve [10–13]. A negative mask removes material from FEs over which it lays [4, 8], whereas a positive mask retain material beneath it [13, 14]. We use negative elliptical masks wherein each mask is defined using seven variables: x_j , y_j , a_j , b_j , θ_j , α_j , and γ_j . The first five is called geometrical variables and latter two are termed material variables, positive valued, of a mask. FEs that are close to but outside mask j boundary with high α_j tend to achieve material density $\rho \approx 1$ (Fig. 1b). Likewise, higher γ_j makes FEs situated just outside and/or within mask j loose more material thus making their $\rho \approx 0$ (Fig. 1c). Therefore, α_j is called material dilation variable, whereas γ_j is named material erosion variable. Fig. 1 demonstrates material density plots for the FEs. The effects of α_j and γ_j on the material distribution layout wherein widths of the masks indicate values of respective α_j and γ_j are indicated in Fig. 1b and 1c respectively. In this work, we systematically determine α_j and γ_j for each negative elliptical mask in addition to the latter’s geometrical variables such that optimized, close to 0-1 topologies can be obtained with an explicit gray-scale constraint.

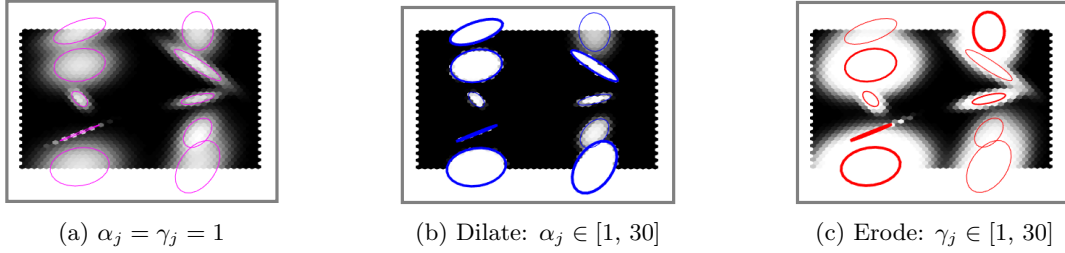


Figure 1: Effect of α_j and γ_j on material density of FEs. (a) Design with $\alpha_j = 1$ and $\gamma_j = 1$. The design in (a) is processed by randomly varying α_j and γ_j to demonstrate their effect. (b) $\alpha_j \in [1, 30]$ are randomly varied keeping $\gamma_j = 1$. (c). $\gamma_j \in [1, 30]$ are randomly varied keeping $\alpha_j = 1$. The line widths of masks in (b) and (c) are as per their α_j and γ_j .

Compliant mechanisms (CMs) are monolithic designs that utilize their flexible (compliant) members to perform their tasks in response to input actuations and can find various applications with/without pressure loads in [15–17] and references therein. Only a few TO approaches for pressure-actuated CMs can be found [2] and in those, none of them yet is presented to achieve such optimized mechanism with 0-1 designs. With above improved material assignment for a mask, we not only seek geometrical singularities free, close to black and white pressure-actuated CMs but also, pressure-loaded structures. For the former, a multi-criteria [18] objective is minimized, whereas compliance is minimized for the latter. Figure 2 illustrates schematic diagrams for a pressure loadbearing structure and a pressure-actuated CM. It can be seen that pressure loading surface has moved from its initial surface Γ_p to the final surface Γ_{pb} (cf. Fig. 2a and 2b). Next, we summarize existing approaches in TO for pressure-loaded designs.

The first TO approach involving pressure loads was presented by Hammer and Olhoff [1] for designing loadbearing structures by minimizing compliance. Du and Olhoff [19] further modified the method presented in [1]. Fuchs and Shemesh [20] employed additional variables for pressure loading boundaries. An element-based approach was presented by Zhang et al. [21]. Lee and Martins [22] presented an approach which does not require *a priori* data of starting and ending points for pressure curves. Li et al. [23] presented a regional contour tracking algorithm in conjunction with digital image processing. Ibbadode et al. [24] presented an approach with boundary identification and load evolution. One can also find approaches using the level set methods in [25–27].

Instead of locating pressure loading contour explicitly, different alternate approaches were also presented. A fictitious thermal loading concept was used by Chen and Kikuchi [28]. Chen et al. [29] used the method in [28] to design pressure-actuated CMs. A three-phase material (solid, void, and fluid) definition was used by Bourdin and Chambolle [30]. Sigmund and Clausen [31] employed the mixed finite element method¹ with three-phase material description. A pseudo electrical potential technique was employed by Zheng et al. [33]. Vasista and Tong [34] employed the SIMP (Solid Isotropic Material Penalization) and MIST (Moving Isosurface Threshold) methods with the mixed displacement-pressure FE formulation. Panganiban et al. [35] used the displacement-based nonconforming FE approach with three-phase

¹Needs to satisfy the Babuska-Brezzi condition [32]

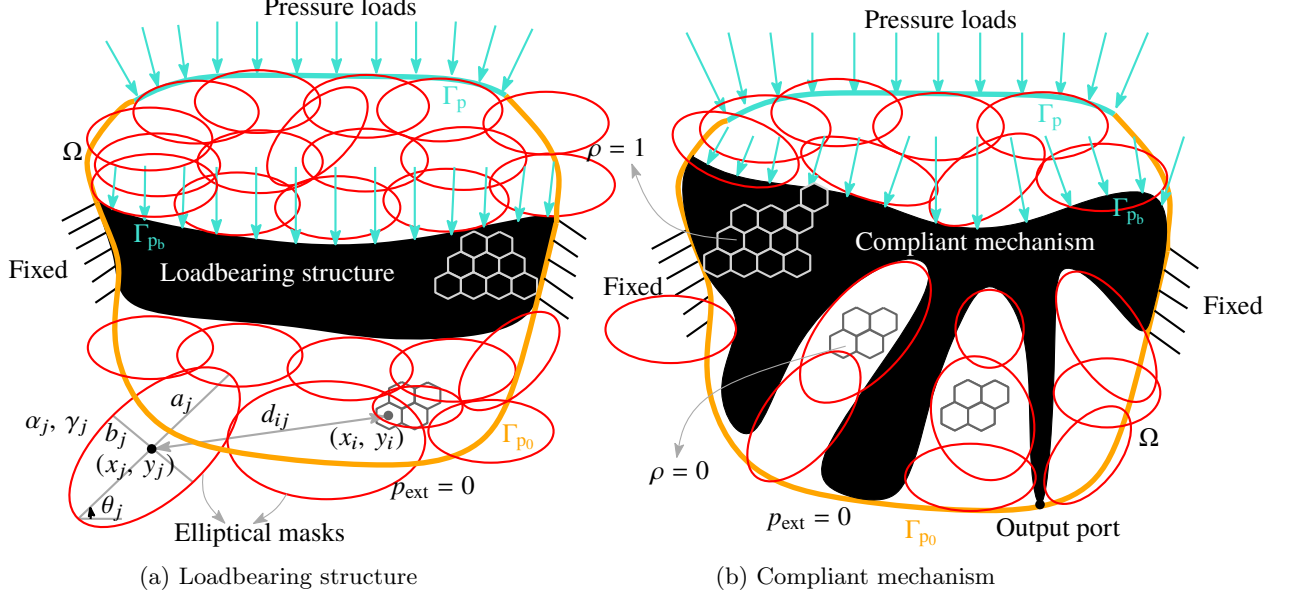


Figure 2: Figure depicts schematic diagrams for a pressure-loaded structure and a pressure-actuated CM in (a) and (b), respectively. The design domain is denoted by Ω , boundaries with finite and zero pressure loads are indicated via Γ_p and Γ_{p_0} respectively and the final boundaries where the pressure is applied is shown by surface Γ_{pb} .

material description, and de Souza and Silva [36] employed method presented in [31] in their approach. Kumar et al. [2] used Darcy's law in association with a drainage term to design both pressure-loaded structures and pressure-actuated CMs. Herein, we adopt the method presented in [2] for pressure-field modeling.

In summary, the current manuscript offers following new aspects:

- A Material Masks Overlay Strategy topology optimization approach to achieve optimized, close to black-and-white pressure-loaded structures and pressure-actuated compliant mechanisms,
- Formulation of negative elliptical masks with material erosion and dilation variables to assign material density within each hexagonal FE,
- Implicitly detecting pressure loading surface using the Darcy law with hexagonal element description of the design domain in line with [2]
- Explicitly using a gray-scale measure constraint to ensure pressure-loaded topologies close to 0-1 solutions.

The remainder of the paper is organized as follows. Section 2 describes density material modeling using negative elliptical masks for an FE. Section 3 presents pressure modeling including methodology, finite element formulation, calculation of the nodal forces and verification problems. Topology optimization formulation, objective functions employed for the loadbearing structures and CMs under used volume and gray scale constraints and sensitivity analysis are presented in Section 4. Section 5 reports numerical examples for structure and CM designs, and pertaining discussions. Lastly, conclusions are drawn in Section 6.

2 Material density modeling

In a typical TO setting with regular² FE discretization descriptions, each FE is assigned a material density ρ . Such variables (ideally) attain either 0 or 1 values at the end of optimization and thus, help decide the final material layout of the optimized designs. Herein, a set of negative elliptical masks are employed to determine material density of hexagonal FEs which are used to describe the given design domain. The final position, shape, size, orientation, material dilation and erosion variables of masks determine the optimized material layout wherein the density of the i^{th} hexagonal FE with respect to the j^{th} elliptical mask, i.e., ρ_{ij} is computed using the logistic approximation of Heaviside function as [13]

$$\rho_{ij}(\alpha_j) = \left[\frac{1}{1 + \exp(-\alpha_j d_{ij})} \right], \quad (1)$$

where d_{ij} , a Euclidean distance measure, determines position of the centroid of the i^{th} FE with respect to that of the j^{th} mask (cf. Fig. 2). α_j , material dilation variable, influences the binary nature of the solutions (Fig. 1b). Mathematically, d_{ij} is evaluated as (Fig. 2)

$$d_{ij} = \left(\frac{X_{ij}}{a_j} \right)^2 + \left(\frac{Y_{ij}}{b_j} \right)^2 - 1, \quad (2)$$

with,

$$\begin{pmatrix} X_{ij} \\ Y_{ij} \end{pmatrix} = \begin{bmatrix} \cos \theta_j & \sin \theta_j \\ -\sin \theta_j & \cos \theta_j \end{bmatrix} \begin{pmatrix} x_i - x_j \\ y_i - y_j \end{pmatrix}, \quad (3)$$

where (x_i, y_i) and (x_j, y_j) are center coordinates of the i^{th} hexagonal FE and j^{th} elliptical mask. a_j and b_j represent the semi-major and -minor axes of the mask and θ_j is its orientation with respect to the horizontal direction. Note that the lower and upper limits for a_j and b_j can be defined based on the dimension of an FE and design, and $\theta_j \in [-\frac{\pi}{2}, \frac{\pi}{2}]$.

In view of m_n such masks, one writes the material density of the i^{th} FE as

$$\rho_i(\alpha_j, \gamma_j) = \prod_{j=1}^{m_n} \left[\frac{1}{1 + \exp(-\alpha_j d_{ij})} \right]^{\gamma_j}, \quad (4)$$

where γ_j , material erosion variable, $\in [\gamma_l, \gamma_u]$ and $\alpha_j \in [\alpha_l, \alpha_u]$. α_j and γ_j together, can steer the material density of an FE towards either 0 or 1 and thus, helping to ensure crisp final solutions. γ_l and γ_u are user defined lower and upper bounds on γ_j . Likewise, α_l and α_u represent lower and upper limits for α_j . Let $\psi_j = \{x_j, y_j, a_j, b_j, \theta_j, \alpha_j, \gamma_j\}$. Negative masks can also be used to generate contact surfaces within them while designing contact-aided designs [37, 38].

3 Pressure loads modeling

Darcy's law in association with a volumetric material-dependent pressure loss, i.e., drainage term, is employed to relate the pressure field with material density vector $\boldsymbol{\rho}$. The associated PDE is solved using the standard finite element formulation using Wachspress shape functions [39]. The formulation facilitates implicit detection of the pressure loading surface and conversion of the obtained pressured field into the consistent hexagonal FE nodal forces.

3.1 Methodology

We describe the Darcy law, the drainage term and associated parameters in brief, and of that a detailed description can be found in [2]. The Darcy law that helps finding pressure field through a porous medium

²In case of irregular FE discretization, in general, nodal design variables are preferred to avoid favoring one FE over others by TO.

is adopted wherein the Darcy flux \mathbf{q} depends upon the pressure gradient ∇p , the fluid viscosity μ and permeability of the medium κ as

$$\mathbf{q} = -\frac{\kappa}{\mu} \nabla p = -K \nabla p, \quad (5)$$

where K represents the flow coefficient that refers to the ability to allow fluid to pass through a porous medium. To cater for a TO setting, each material-phase of an FE is also associated with one flow coefficient, and the actual flow coefficient of an FE is determined by performing interpolation between those associated to its solid and void material states using a smooth Heaviside projection function as

$$K(\rho_i(\psi_j)) = K_V(1 - (1 - \epsilon))H_K(\rho_i(\psi_j), \eta_K, \beta_K), \quad (6)$$

where $\epsilon = \frac{K_S}{K_V}$ is the flow contrast [40] wherein K_S and K_V are the flow coefficients for solid and void phased FEs, respectively. $H_K(\rho_i, \eta_K, \beta_K)$ indicates a smooth Heaviside projection function defined as

$$H_K(\rho_i(\psi_j), \eta_K, \beta_K) = \left(\frac{\tanh(\beta_K \eta_K) + \tanh(\beta_K(\rho_i - \eta_K))}{\tanh(\beta_K \eta_K) + \tanh(\beta_K(1 - \eta_K))} \right), \quad (7)$$

where η_K and β_K help control position of the step and slope of $K(\rho_i(\psi_j))$ respectively. $\rho_i(\psi_j)$ is evaluated using Eq. (4) indicating that the defined flow coefficient $K(\rho_i(\psi_j))$ depends upon the position, shape, size, orientation, material dilation and erosion variables of the masks employed in TO. In a typical TO setting, using Darcy's law alone may fail to ensure the desire pressure field for a reasonable design as it provides pressure gradient throughout the design domain (see Fig. 5a). Therefore, a drainage term conceptualized in [2] is employed to ensure a sharp and continuous pressure drop as soon as pressure loads encounter a solid FE while TO progresses (see Fig. 5d and Fig. 5e), i.e., drainage term becomes active when pressure loads faces solid FEs otherwise remains inactive. Q_{drain} is defined as

$$Q_{\text{drain}} = -D(\rho_i(\psi_j))(p - p_{\text{ext}}), \quad (8)$$

where the pressure field and external pressure are indicated via p and p_{ext} , respectively and $D(\rho_i)$ is the drainage coefficient defined using a smooth Heaviside function as

$$D(\rho_i(\psi_j)) = D_S H_D(\rho_i(\psi_j), \eta_D, \beta_D), \quad (9)$$

where η_D and β_D are adaptable parameters and $H_D(\rho_i(\psi_j), \eta_D, \beta_D)$ is analogous to that mentioned in Eq. (7). D_S is the drainage coefficient of a solid hexagonal FE that controls the pressure-penetration depth and is determined in terms of K_S as [2]

$$D_S = \left(\frac{\ln r}{\Delta s} \right)^2 K_S, \quad (10)$$

where $r = \frac{p|_{\Delta s}}{p_{\text{in}}}$; Δs , a penetration parameter, is set to equal to width/height of a few FEs, and p_{in} and $p|_{\Delta s}$ are input pressure and pressure at Δs respectively.

3.2 Finite element formulation for pressure loading

The basic balance equation for Darcy's law in conjunction with Q_{drain} and incompressible fluid flow assumptions can be written as [2]

$$\nabla \cdot \mathbf{q} - Q_{\text{drain}} = 0, \quad (11)$$

In view of Eq. (5), Eq. (11) yields to

$$\nabla \cdot (K \nabla p) + Q_{\text{drain}} = 0. \quad (12)$$

The PDE in Eq. (12) is solved to evaluate pressure field using the Galerkin method of finite element formulation as

$$\sum_{i=1}^{Nel} \left(\int_{\Omega_i} \nabla \cdot (K \nabla p) G \, dV + \int_{\Omega_i} Q_{\text{drain}} G \, dV \right) = 0, \quad (13)$$

where N_{el} indicates the total number of hexagonal FEs employed to describe the design domain Ω , $\Omega_i|_{i=1,2,3,\dots,N_{el}}$ represent hexagonal FEs, dV is the elemental volume, and G is determined using the same basis functions that are employed for interpolating pressure. For a hexagonal FE

$$p = \mathbf{N}_p \mathbf{p}_i, \quad \text{and} \quad G = \mathbf{N}_p \mathbf{G}_i, \quad (14)$$

where $\mathbf{p}_i = [p_1, p_2, p_3, p_4, p_5, p_6]^T$ are the hexagonal nodal pressures and $\mathbf{N}_p = [N_1, N_2, N_3, N_4, N_5, N_6]$ are the Wachspress shape functions (see Appendix A). Using integration by parts, divergence theorem and Eq. (14), one writes Eq. (13) as

$$\int_{\Omega_i} \left(K \mathbf{B}_p^T \mathbf{B}_p + D \mathbf{N}_p^T \mathbf{N}_p \right) dV \mathbf{p}_i = \int_{\Omega_i} D \mathbf{N}_p^T p_{\text{ext}} dV - \int_{\Gamma_i} \mathbf{N}_p^T \mathbf{q}_\Gamma \cdot \mathbf{n}_i dA \quad (15)$$

$$\mathbf{A}_i \mathbf{p}_i = \mathbf{f}_i$$

where the flux through the boundary Γ_i is represented via \mathbf{q}_Γ , $\mathbf{B}_p = \nabla \mathbf{N}_p$, \mathbf{n}_i indicates the outward normal to the surface Γ_i , and dA is the elemental area. Eq. (15) transpires in global sense to

$$\mathbf{A} \mathbf{p} = \mathbf{f}. \quad (16)$$

The global flow matrix \mathbf{A} , the global pressure vector \mathbf{p} and the global loading vector \mathbf{f} are obtained by assembling corresponding elemental \mathbf{A}_i , \mathbf{p}_i and \mathbf{f}_i , respectively. In this work, p_{ext} and \mathbf{q}_Γ are set to zero, therefore, $\mathbf{A} \mathbf{p} = \mathbf{0}$ is solved to evaluate pressure field with given pressure loads at input locations. Each node has only one degree of freedom corresponding to pressure load and thus, it is computationally cheap to solve. The global hexagonal nodal forces \mathbf{F} are determined as

$$\mathbf{F} = -\mathbf{T} \mathbf{p}, \quad (17)$$

where \mathbf{T} is a transformation matrix evaluated by assembling elemental \mathbf{T}_i determined as [2]

$$\mathbf{T}_i = - \int_{\Omega_i} \mathbf{N}_u^T \mathbf{B}_p dV, \quad (18)$$

where $\mathbf{N}_u = [N_1 \mathbf{I}, N_2 \mathbf{I}, N_3 \mathbf{I}, N_4 \mathbf{I}, N_5 \mathbf{I}, N_6 \mathbf{I}]$, $N_l|_{l=1,2,\dots,6}$ are Wachspress shape functions and \mathbf{I} is the identity matrix in \mathcal{R}^2 . Integrations in Eqs. (15) and (18) are evaluated using the quadrature rule mentioned in Appendix B.

3.3 Pressure modeling verification

To demonstrate of the employed pressure modeling scheme (Sec. 3) with hexagonal FEs simulated using Wachspress shape functions, we consider two design domains: DDomain I (Fig. 4a) and DDomain II (Fig. 4b) with respective pressure and structural boundary conditions (Fig. 4). Each hexagonal FE of DDomain I is assigned low material density $\rho = 0.01$. DDomain II is with two solid material regions which are introduced to illustrate behavior of the drainage term (Eq. 9). $\rho = 0.01$ is assigned to each FE associated to the remaining domain of DDomain II. The bottom edge of DDomain I experiences pressure loading, whereas its remaining edges are kept at zero pressure loading. In DDomain II, the top and bottom edges experience zero and full pressure loading, respectively. Other specifications are indicated in Table 1. The employed scales for material density field and pressure field in this paper are plotted in Fig. 3a and Fig. 3b, respectively. Plane-stress conditions are considered herein for all other design problems reported in this paper.

The pressure field obtained by solving Eq. (15) is depicted in Fig. 5a for DDomain I, and that for DDomain II without and with drainage term are plotted in Fig. 5b and Fig. 5d, respectively. Fig. 5c and Fig. 5e indicate the pressure field with solid material layers. One notices that pressure gradient exists throughout within DDomain I, which is expected as per Darcy's law. The material density for each FE in DDomain I is kept low ($\rho = 0.01$) consequently, drainage term (Eq. 9) remains always inactive. One notices without drainage term the obtained pressure field is not realistic for DDomain II (Fig. 5b and Fig. 5c), whereas Fig. 5d and Fig. 5e indicate the desired pressure field and thus, the conceptualized drainage term is indeed essential. The obtained pressure fields of DDomain II with and without drainage term are converted into the nodal force using Eq. 17.

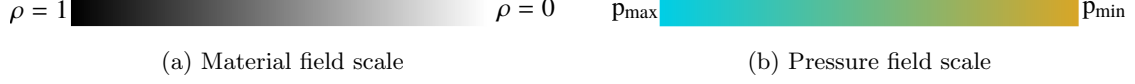


Figure 3: Scales for the material density field and pressure field are displayed in (a) and (b), respectively, that are employed in this paper to show the optimized results and final pressure field. $p_{\max} = 1$ bar and $p_{\min} = 0$ bar unless otherwise stated.

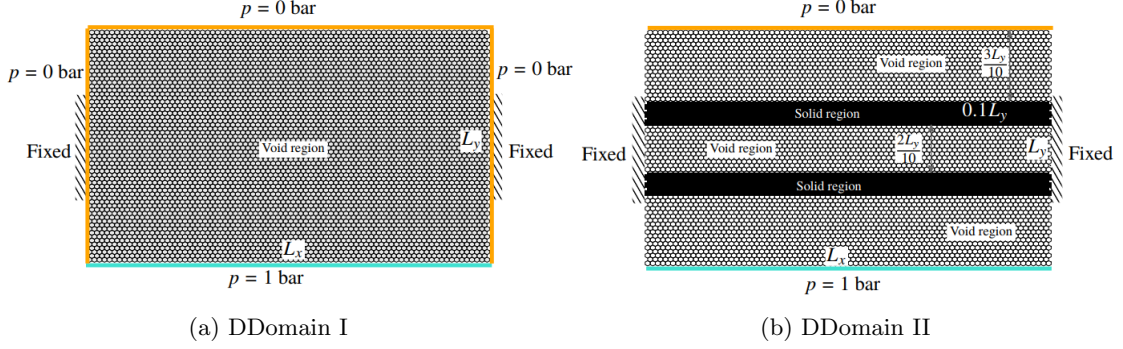


Figure 4: Design domains DDomain I and DDomain II are depicted in (a) and (b), respectively. Material density of each FE in (a) is set to 0.01. $L_x = 0.2 \cos(\frac{\pi}{6})$ m, and $L_y = 0.2 \sin(\frac{\pi}{6})$ m, designs are parameterized using 80×60 FEs. DDomain II has two solid FE (dark) layers of width $0.1L_y$ separated by $0.2L_y$. Fixed locations, pressure and zero pressure loadings edges are shown.

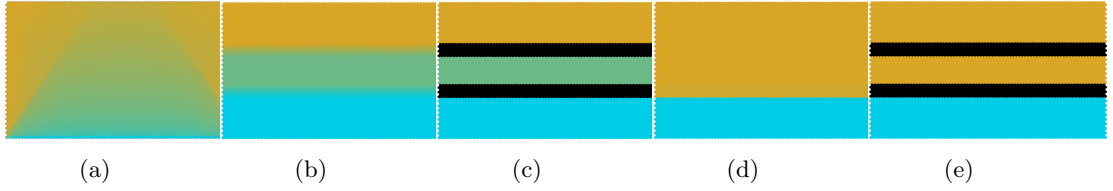


Figure 5: Pressure fields for DDomain I and DDomain II are displayed. (a) DDomain I pressure field (b) DDomain II pressure field without drainage term is plotted without solid regions (c) DDomain II pressure field without drainage term with solid regions, (d) DDomain II pressure field with drainage term without solid regions and (e) DDomain II pressure field with drainage term with solid regions. One notice that the gradient of pressure field gets confined as soon as it faces the first solid region in DDomain when using the drainage term (Fig. 5d and Fig. 5e), however the same is not noted without the drainage term (Fig. 5b and Fig. 5c).

4 Optimization problem formulation

This section presents the optimization problem formulation and pertaining sensitivity analysis of the objectives employed for designing pressure loadbearing structures and pressure-actuated CMs.

Let ψ be the design vector stacks seven variables $(x_j, y_j, a_j, b_j, \theta_j, \alpha_j, \gamma_j |_{j=1, \dots, m_n})$ which define each mask. The material densities of all FEs stacked in a vector, as per Eq. 4 a function of ψ , is denoted via ρ . The following optimizations problem are solved:

$$\left. \begin{array}{l}
\begin{array}{c} \text{Structures} \\ \min_{\boldsymbol{\rho}(\boldsymbol{\psi})} (f_s^0 = 2SE) \end{array} \\
\begin{array}{c} \text{Compliant Mechanisms} \\ \min_{\boldsymbol{\rho}(\boldsymbol{\psi})} \left(f_{\text{CM}}^0 = -\chi \frac{MSE}{SE} \right) \end{array} \\
\text{s.t.} \quad \mathbf{K}(\boldsymbol{\rho}(\boldsymbol{\psi}))\mathbf{v} = \mathbf{F}_d \\
\mathbf{A}(\boldsymbol{\rho}(\boldsymbol{\psi}))\mathbf{p} = \mathbf{0} \\
\mathbf{K}(\boldsymbol{\rho}(\boldsymbol{\psi}))\mathbf{u} = \mathbf{F} = -\mathbf{T}(\boldsymbol{\rho}(\boldsymbol{\psi}))\mathbf{p} \\
g_1 = \frac{V(\boldsymbol{\rho}(\boldsymbol{\psi}))}{V^*} - 1 \leq 0 \\
g_2 = GS_I = \frac{\sum_{i=1}^{Nel} 4\rho_i(1 - \rho_i)}{Nel} \leq \delta \\
\boldsymbol{\psi} = [x_j, y_j, a_j, b_j, \theta_j, \alpha_j, \gamma_j]_{j=1, \dots, m_n} \\
\boldsymbol{\psi}_{\min} \leq \boldsymbol{\psi} \leq \boldsymbol{\psi}_{\max}
\end{array} \right\}, \quad (19)$$

where SE and $MSE = \mathbf{v}^\top \mathbf{K} \mathbf{u}$ represent strain energy and mutual-strain energy, respectively. \mathbf{u} determined using $\mathbf{K}(\boldsymbol{\rho}(\boldsymbol{\psi}))\mathbf{u} = \mathbf{F}$, and \mathbf{v} evaluated employing³ $\mathbf{K}(\boldsymbol{\rho}(\boldsymbol{\psi}))\mathbf{v} = \mathbf{F}_d$, are the global displacement vectors corresponding to the forces \mathbf{F} and \mathbf{F}_d . \mathbf{F}_d is a dummy unit force applied in the direction of the desired output deformation of the CMs, whereas \mathbf{F} is evaluated using Eq. (17). \mathbf{K} is the global stiffness matrix of the design domain evaluated by assembling elemental stiffness $\mathbf{k}_i = [E_{\min} + \rho_i(\alpha_j, \gamma_j)(E_1 - E_{\min})] \mathbf{k}_0$, E_1 and E_{\min} are the Young's moduli of a solid and void FE, respectively, $\rho_i(\alpha_j, \gamma_j)$ is the material density of the i^{th} FE (Eq. 4) and \mathbf{k}_0 is the elemental stiffness matrix for a solid FE at unit elastic modulus. Further, χ , a consistent scaling factor, is primarily employed to adjust sensitivities of the objective pertaining to CMs [18]. g_1 , an inequality constraint, guides to achieve the optimized design with the permitted resource volume. $V(\boldsymbol{\rho}(\boldsymbol{\psi}))$ and V^* indicate the current and permitted volumes of the design domain, respectively. g_2 is the gray scale indicator [41] constraint and δ is a user defined (very) small positive number. This constraint is applied to ensure that optimized designs get motivated towards 0-1 solutions with α_j and γ_j as additional design variables. \mathbf{A} , \mathbf{T} and \mathbf{p} represent the global flow matrix, global transformation matrix, and global pressure loads vector, respectively. $\boldsymbol{\psi}_{\min}$ and $\boldsymbol{\psi}_{\max}$ are the lower and upper limits on the design vector $\boldsymbol{\psi}$ respectively.

4.1 Sensitivity analysis

The method of moving asymptotes (MMA) [42], a gradient-based optimizer, is used herein to solve the optimization problems, therefore one requires to have sensitivities of the objective(s) and constraint(s) with respect to design vector $\boldsymbol{\psi}$ for the optimization. One notes (Eq. 19), objectives (SE and $-\frac{MSE}{SE}$) and constraints are function of the material density vector $\boldsymbol{\rho}$ and that depends upon $\boldsymbol{\psi}$, therefore a chain rule is employed for determining the sensitivities, which is described below.

Let ψ_j^1 represents any one of the $\{x_j, y_j, a_j, b_j, \theta_j\}$ and $\psi_j = \{\psi_j^1, \alpha_j, \gamma_j\}$. Using Eq. (4), derivative of ρ_i with respect to ψ_j^1 can be evaluated as

$$\frac{\partial \rho_i(\alpha_j, \gamma_j)}{\partial \psi_j^1} = \gamma_j \alpha_j \rho_i(\alpha_j, \gamma_j) \left[1 - \frac{1}{1 + \exp(-\alpha_j d_{ij})} \right] \left[\frac{\partial d_{ij}}{\partial \psi_j^1} \right], \quad (20)$$

where $\left[\frac{\partial d_{ij}}{\partial \psi_j^1} \right]$ are evaluated using Eq. 2 and Eq. 3 as

³ $\mathbf{K}(\boldsymbol{\rho}(\boldsymbol{\psi}))\mathbf{v} = \mathbf{F}_d$ is solved only while designing CMs.

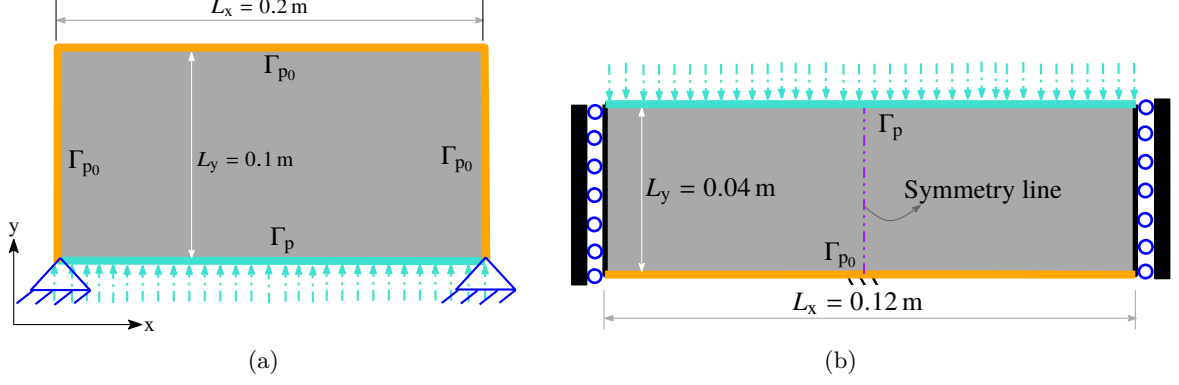


Figure 6: Figure displays the design domains for Internally pressurized and piston loadbearing structures in (a) and (b) respectively.

$$\left. \begin{aligned} \frac{\partial d_{ij}}{\partial x_j} &= 2 \left[- \left(\frac{X_{ij}}{a_j} \right) \left(\frac{\cos \theta_j}{a_j} \right) + \left(\frac{Y_{ij}}{b_j} \right) \left(\frac{\sin \theta_j}{b_j} \right) \right] \\ \frac{\partial d_{ij}}{\partial y_j} &= -2 \left[\left(\frac{X_{ij}}{a_j} \right) \left(\frac{\sin \theta_j}{a_j} \right) + \left(\frac{Y_{ij}}{b_j} \right) \left(\frac{\cos \theta_j}{b_j} \right) \right] \\ \frac{\partial d_{ij}}{\partial a_j} &= -2 \frac{X_{ij}^2}{a_j^3}, \quad \frac{\partial d_{ij}}{\partial b_j} = -2 \frac{Y_{ij}^2}{b_j^3} \\ \frac{\partial d_{ij}}{\partial \theta_j} &= 2 \left(\frac{X_{ij} Y_{ij}}{a_j^2} - \frac{X_{ij} Y_{ij}}{b_j^2} \right) \end{aligned} \right\}. \quad (21)$$

Derivatives of $\rho_i(\alpha_j, \gamma_j)$ with variables α_j and γ_j can be found as

$$\frac{\partial \rho_i(\alpha_j, \gamma_j)}{\partial \alpha_j} = \gamma_j d_{ij} \rho_i(\alpha_j, \gamma_j) \left[1 - \frac{1}{1 + \exp(-\alpha_j d_{ij})} \right], \quad (22)$$

$$\frac{\partial \rho_i(\alpha_j, \gamma_j)}{\partial \gamma_j} = \rho_i(\alpha_j, \gamma_j) \log \left(\frac{1}{1 + \exp(-\alpha_j d_{ij})} \right). \quad (23)$$

Therefore, $\frac{\partial \rho_i}{\partial \psi_j} = \left[\left[\frac{\partial \rho_i}{\partial \psi_j} \right]^T \left[\frac{\partial \rho_i(\alpha_j, \gamma_j)}{\partial \alpha_j} \right]^T \left[\frac{\partial \rho_i(\alpha_j, \gamma_j)}{\partial \gamma_j} \right]^T \right]$. The adjoint-variable method is used to evaluate sensitivities of the objectives with respect to the material density vector $\boldsymbol{\rho}$. One writes the following overall performance functions \mathcal{L}_s for loadbearing structures as

$$\mathcal{L}_s = f_s^0 + \boldsymbol{\lambda}_{s1}^T (\mathbf{K}\mathbf{u} + \mathbf{T}\mathbf{p}) + \boldsymbol{\lambda}_{s2}^T (\mathbf{A}\mathbf{p}), \quad (24)$$

where $\boldsymbol{\lambda}_{s1}$ and $\boldsymbol{\lambda}_{s2}$ are the Lagrange multiplier vectors. Likewise, the performance function \mathcal{L}_{CM} for CMs is

$$\mathcal{L}_{CM} = f_{CM}^0 + \boldsymbol{\lambda}_{CM1}^T (\mathbf{K}\mathbf{u} + \mathbf{T}\mathbf{p}) + \boldsymbol{\lambda}_{CM2}^T (\mathbf{A}\mathbf{p}) + \boldsymbol{\lambda}_{CM3}^T (\mathbf{K}\mathbf{v} - \mathbf{F}_d), \quad (25)$$

where $\boldsymbol{\lambda}_{CM1}$, $\boldsymbol{\lambda}_{CM2}$ and $\boldsymbol{\lambda}_{CM3}$ are the Lagrange multiplier vectors. These multipliers can be determined as [2]

$$\left. \begin{aligned} \boldsymbol{\lambda}_{s1}^T &= -\frac{\partial f_s^0}{\partial \mathbf{u}} \mathbf{K}^{-1} = -2\mathbf{u}^T \\ \boldsymbol{\lambda}_{s2}^T &= -\boldsymbol{\lambda}_{s1}^T \mathbf{T} \mathbf{A}^{-1} = 2\mathbf{u}^T \mathbf{T} \mathbf{A}^{-1} \end{aligned} \right\}, \quad (26)$$

and

$$\left. \begin{aligned} \boldsymbol{\lambda}_{CM1}^T &= -\frac{\partial f_{CM}^0}{\partial \mathbf{u}} \mathbf{K}^{-1} = \chi \left(\frac{\mathbf{v}^T}{SE} - \mathbf{u}^T \frac{MSE}{(SE)^2} \right) \\ \boldsymbol{\lambda}_{CM2}^T &= -\boldsymbol{\lambda}_{CM1}^T \mathbf{T} \mathbf{A}^{-1} = -\chi \left(\frac{\mathbf{v}^T}{SE} - \mathbf{u}^T \frac{MSE}{SE} \right) \mathbf{T} \mathbf{A}^{-1} \\ \boldsymbol{\lambda}_{CM3}^T &= -\frac{\partial f_{CM}^0}{\partial \mathbf{v}} \mathbf{K}^{-1} = \chi \frac{\mathbf{u}^T}{SE} \end{aligned} \right\}. \quad (27)$$

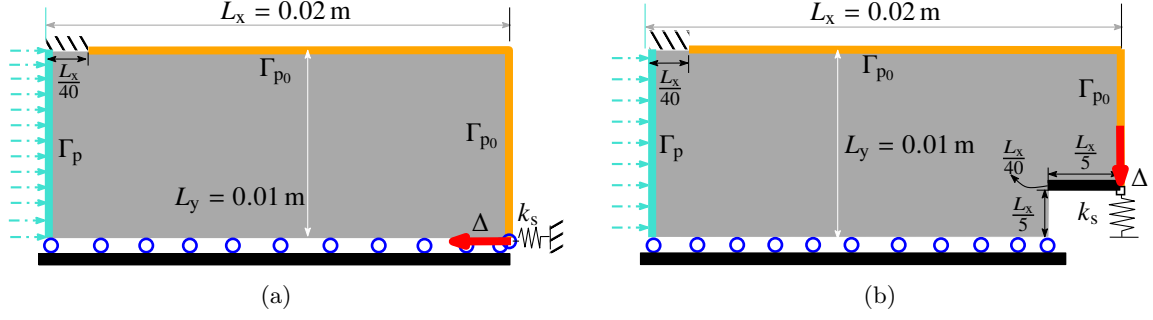


Figure 7: Figure displays the design domains for CMs. (a) Inverter mechanism design domain and (b) Gripper mechanism design domain.

Table 1: Details of parameters used

| Nomenclature | Symbol | Value |
|--|-----------------|--|
| <i>Masks parameters</i> | | |
| No. of Masks in x -direction | N_{mx} | 20 |
| No. of masks in y -direction | N_{my} | 10 |
| Mask radius parameter | mR | $20 \times \text{edge-length of an FE}$ |
| Lower bound factor for the axes of a mask | f_l | $0.1 \times mR$ |
| Upper bound factor for the axes of a mask | f_u | $1 \times mR$ |
| lower bounds for α_j and γ_j | – | 1, 1 |
| Upper bounds for α_j and γ_j | – | 20, 10 |
| <i>Material Parameters</i> | | |
| Young's modulus of a solid FE | E_1 | $5 \times 10^8 \text{ N m}^{-2}$ |
| Young's modulus of a void FE | E_{\min} | $E_1 \times 10^{-6}$ |
| SIMP penalty parameter | ζ | 1 |
| <i>Pressure load parameters</i> | | |
| Input pressure load | p_{in} | $1 \times 10^5 \text{ N m}^{-2}$ |
| $K(\rho)$ step location | η_k | 0.3 |
| $K(\rho)$ step location | β_k | 10 |
| $D(\rho)$ step location | η_h | 0.3 |
| $D(\rho)$ step location | β_h | 10 |
| Flow coefficient of a void FE | K_v | $1 \text{ m}^4 \text{ N}^{-1} \text{ s}^{-1}$ |
| Flow coefficient of a solid FE | K_s | $K_v \times 10^{-7} \text{ m}^4 \text{ N}^{-1} \text{ s}^{-1}$ |
| Drainage from solid | D_s | $\left(\frac{\ln r}{\Delta s}\right)^2 K_s$ |
| Remainder of input pressure at Δs | r | 0.1 |

Using Eqs. (24), (25), (26) and (27), sensitivities of the objective functions with respect to ρ can be written as

$$\left. \begin{aligned}
\frac{df_s^0}{d\boldsymbol{\rho}} &= \frac{\partial f_s^0}{\partial \boldsymbol{\rho}} + \boldsymbol{\lambda}_{s1}^\top \frac{\partial \mathbf{K}}{\partial \boldsymbol{\rho}} \mathbf{u} + \boldsymbol{\lambda}_{s2}^\top \frac{\partial \mathbf{A}}{\partial \boldsymbol{\rho}} \mathbf{p} = -\mathbf{u}^\top \frac{\partial \mathbf{K}}{\partial \boldsymbol{\rho}} \mathbf{u} + \underbrace{2\mathbf{u}^\top \mathbf{T} \mathbf{A}^{-1} \frac{\partial \mathbf{A}}{\partial \boldsymbol{\rho}} \mathbf{p}}_{\text{Load sensitivities}} \\
\text{and} \\
\frac{df_{\text{CM}}^0}{d\boldsymbol{\rho}} &= \frac{\partial f_{\text{CM}}^0}{\partial \boldsymbol{\rho}} + \boldsymbol{\lambda}_{\text{CM}1}^\top \frac{\partial \mathbf{K}}{\partial \boldsymbol{\rho}} \mathbf{u} + \boldsymbol{\lambda}_{\text{CM}2}^\top \frac{\partial \mathbf{A}}{\partial \boldsymbol{\rho}} \mathbf{p} + \boldsymbol{\lambda}_{\text{CM}3}^\top \frac{\partial \mathbf{K}}{\partial \boldsymbol{\rho}} \mathbf{v} \\
&= \chi \left[\mathbf{u}^\top \frac{\partial \mathbf{K}}{\partial \boldsymbol{\rho}} \left(\frac{MSE}{(SE)^2} \left(-\frac{\mathbf{u}}{2} \right) + \frac{\mathbf{v}}{SE} \right) \right] + \chi \left[\underbrace{\left(\frac{MSE}{(SE)^2} (\mathbf{u}^\top) + \frac{-\mathbf{v}^\top}{SE} \right) \mathbf{T} \mathbf{A}^{-1} \frac{\partial \mathbf{A}}{\partial \boldsymbol{\rho}} \mathbf{p}}_{\text{Load sensitivities}} \right]
\end{aligned} \right\}, \quad (28)$$

Finally, one employs a chain rule in view with Eqs. (20) and (28) to determine derivatives of the objective functions with respect to design vector $\boldsymbol{\psi}$ as

$$\frac{df_t^0}{d\boldsymbol{\psi}}|_{t=S, \text{CM}} = \frac{\partial f_t}{\partial \boldsymbol{\rho}} \frac{\partial \boldsymbol{\rho}}{\partial \boldsymbol{\psi}}. \quad (29)$$

and thus, the associated load sensitivities get evaluated computationally cheaply. Likewise, sensitivities of the constraints are determined.

5 Numerical examples and discussion

We solve design problems related to loadbearing structures (arch and piston) and CMs (inverter and gripper) involving pressure loads to demonstrate the presented approach. The design domains with known boundary conditions for pressure loading and displacements are depicted in Fig. 6 and 7 for loadbearing structures and CMs, respectively. Γ_p and Γ_{p0} indicate the full and zero pressure loading boundaries, respectively. Optimization parameters and other specifications of the problems are tabulated in Table 1 and any digression is reported in the associated problem definition section. Implementation of the MMA with hexagonal FEs and elliptical masks is same as standard, except that after every MMA iteration one determines the new mask vector/variable as

$$\boldsymbol{\psi}_{\text{new}} = \boldsymbol{\psi}_{\text{old}} + S (\boldsymbol{\psi}_{\text{current}} - \boldsymbol{\psi}_{\text{old}}), \quad (30)$$

where $\boldsymbol{\psi}_{\text{new}}$, $\boldsymbol{\psi}_{\text{old}}$, and $\boldsymbol{\psi}_{\text{current}}$ represent the new, old and current mask design variables. Note $\boldsymbol{\psi}_{\text{current}}$ is the solution obtained from the MMA optimizer using $\boldsymbol{\psi}_{\text{old}}$. S indicates length of a step one requires to multiply that may depend upon types of the problems to be solved. In our experience, $S \in [0.01, 0.1]$ can be a good choice. For all the problems solved, dimensions in x - and y -directions are denoted by L_x and L_y respectively. The number of FEs in x - and y -directions are indicated by N_{ex} and N_{ey} respectively. That for masks are denoted by N_{mx} and N_{my} respectively.

5.1 Internally pressurize arch

TO problem for internally pressurized arch first presented in [1] is solved herein. The design specification is mentioned in Fig. 6a, and Table 1 indicates the design parameters employed. The area the design domain is set to $L_x \times L_y = 0.2 \times 0.1 \text{ m}^2$. The domain is parameterized using $N_{\text{ex}} \times N_{\text{ey}} = 100 \times 50$ hexagonal FEs. $N_{\text{mx}} \times N_{\text{my}} = m_n = 20 \times 10$ elliptical masks are taken for optimization.

5.1.1 Qualifying α_j and γ_j as design variables

We present a study to indicate that considering α_j and γ_j as additional design variables can help achieve close to 0-1 optimized designs. To demonstrate, four cases are conceptualized, CASE I: $\alpha_j|_{j=1,2,\dots,m_n} = 1$ and $\gamma_j = 1$, CASE II: $\alpha_j = 1$ and γ_j are included in the design variables with lower and upper bounds 1 and 10 respectively, CASE III: $\gamma_j = 1$ and α_j are included in the design variables with 1 and 20 as lower and upper bounds respectively, CASE IV: α_j and γ_j are considered design variables with bounds

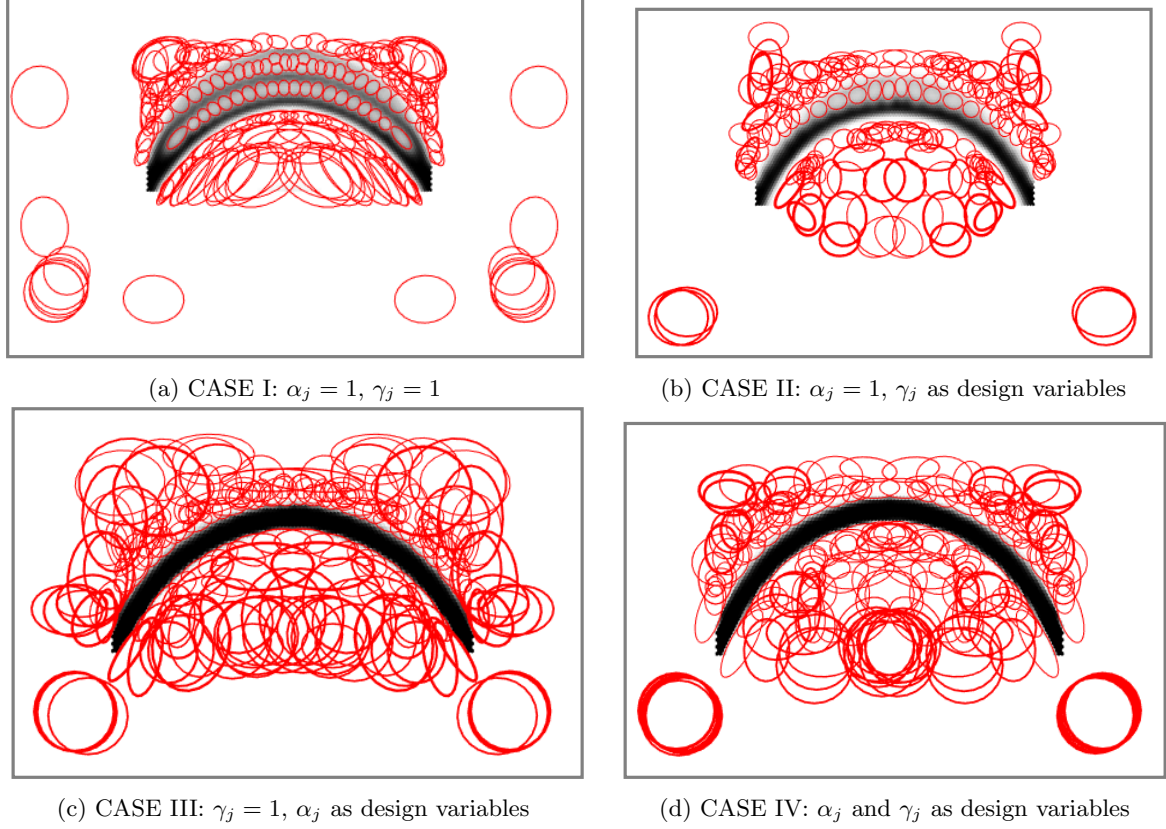


Figure 8: Results for four cases are displayed after 400 MMA iterations. (a) $f_s^0 = 5.261 \text{ N m}$, $V = 20.33\%$, $GS_I = 35.2\%$ (b) $f_s^0 = 6.82 \text{ N m}$, $V = 15.16\%$, $GS_I = 19.72\%$ (c) $f_s^0 = 6.35 \text{ N m}$, $V = 15.96\%$, $GS_I = 6.15\%$ and (d) $f_s^0 = 6.46 \text{ N m}$, $V = 16.30\%$, $GS_I = 5.80\%$. GS_I indicates gray scale indicator.

mentioned in CASE II and CASE III. Constraint g_1 is applied using $V^* = 0.20$. Step length is set to $S = 0.04$ (Eq. 30).

Figure 8 depicts results for all the four cases with respective final normalized compliance values, volume fractions and gray scale indicators GS_I . Results are displayed after 400 MMA iterations. One notices that CASE IV indicates the lowest GS_I value suggesting that the corresponding optimized design has lower gray FEs than others. Though CASE I gives lower final strain energy value, it is difficult to realize that continuum as it has many gray (fictitious material) FEs. To get solutions close to 0-1, we solve the problems henceforth with an additional gray scale indicator GS_I constraint, i.e., with g_2 constraint (Eq. 19).

5.1.2 Arch design

In addition to above design parameters and variables, constraint g_2 (Eq. 19) is considered with δ set to 10^{-3} , i.e., the desired GS_I is 0.1%.

Figures 9, 10a and 10b indicate the optimized designs and convergence history plots for objective, volume fraction and gray scale indicator after 400 MMA iterations respectively. The final shape, size and orientation of masks are displayed with optimized material layout in Fig. 9a and 9b wherein thickness of the masks boundaries are directly proportional to their γ_j and α_j , respectively. Masks with higher γ_j can have lower α_j and vice versa. The exclusive optimized material layout and that with pressure field are shown in Fig. 9c and 9d respectively. Final optimized designs are similar to those obtained in [1, 2]. The optimizer helps achieve the final design such that it can contain the applied pressure loading with minimum compliance. The obtained final normalized compliance, volume fraction and gray scale indicator are 5.34 N m, 0.20% and 0.54% respectively. The volume constraint is satisfied and active

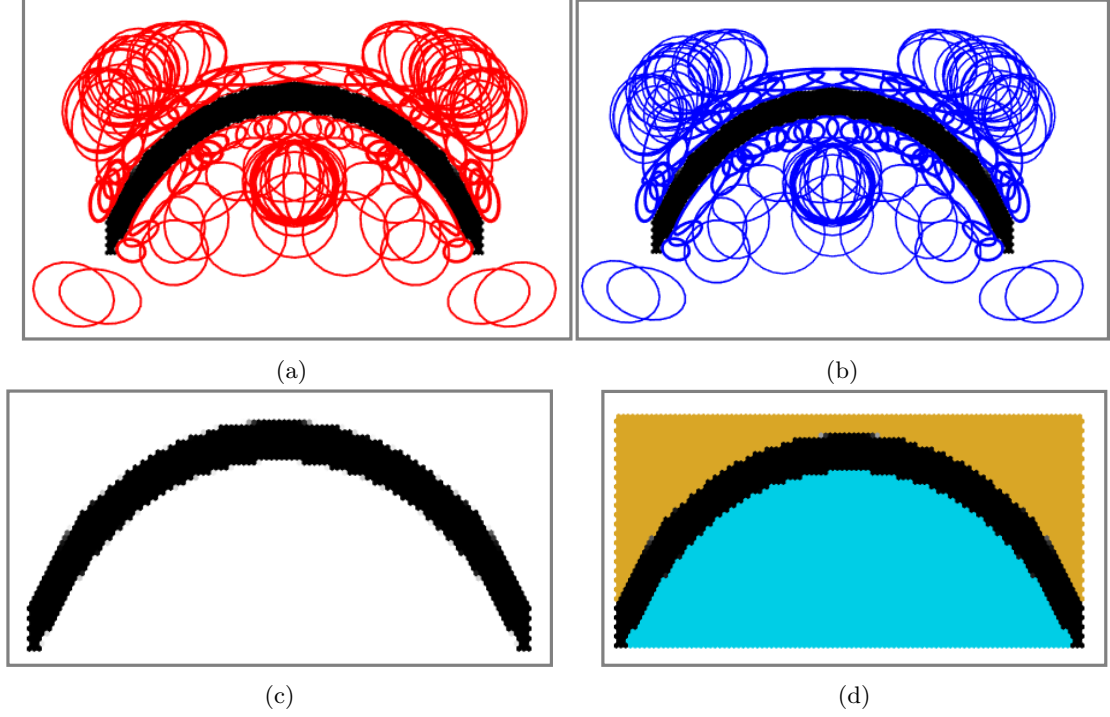


Figure 9: Optimized design for internally pressure loaded arch after 400 MMA iterations (a) Optimized material layout with final elliptical masks whose thickness are proportional to their γ_j , (b) Material layout with final elliptical masks whose thickness are proportional to their α_j , (c) Optimized material layout with $GS_I = 0.54\%$ and (d) Optimized material layout with final pressure field.

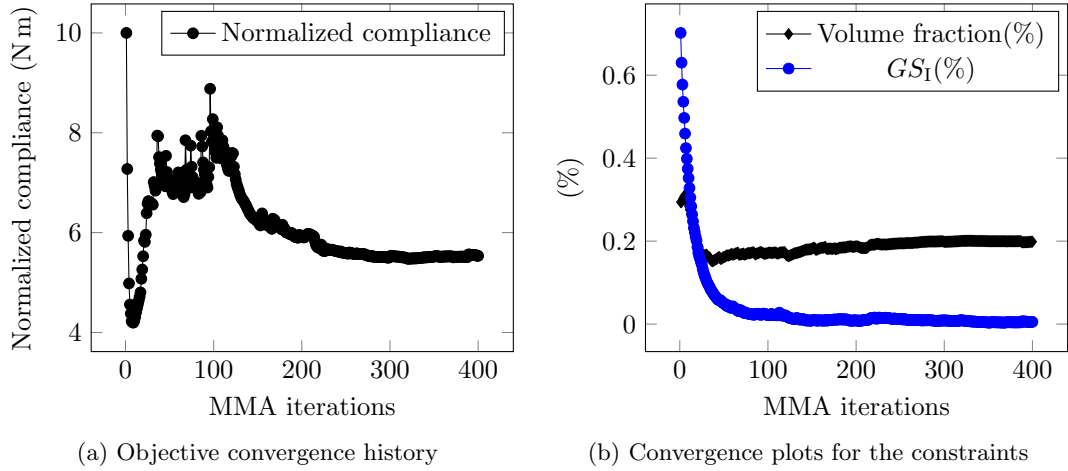


Figure 10: Objective and constraints history for the arch problem.

(Fig. 10b), however gray scale constraint is not satisfied to its desired value of 0.1%. We solve the problem with different gray scale constraint (δ) values (Eq. 19) using same parameters and variables with 100×50 and 200×100 FEs to indicate their effect on the final solutions and tabulate in Table 2. One notes that although a lower δ helps obtain continua closer to 0-1 solutions, the corresponding gray scale constraint does not get satisfied. One also notes from Table 2 that chances of achieving close to the desired/specified δ can increase with mesh refinement. Note that the solutions stays close to the specified constraint boundary. This may be because material density of each FE is a cumulative effect of all mask shapes, sizes, positions and orientations (see Eq. 4). After a limit for a given problem setting with GS_I constraint, it may be difficult for the optimizer to move forward towards a better solution. Further, in view of Fig. 8d and 9c, one notices that using the material dilation and erosion variables alone do not necessarily yield a close to binary solution (Fig. 8d), and that one may need an explicit gray

scale constraint to achieve the same (Fig. 9c). Nevertheless, it can be inferred that the lower gray scale indicator constraint while keeping α_j and γ_j as additional design variables helps in achieving close to 0-1 solutions. In this regard, we prefer to use $\delta = 0.001$ for all the problems. Fig. 10a and 10b illustrate the convergence plots for the objective, volume fraction and gray scale indicator constraint with the MMA iterations. At the end of the optimization, the plots have converging nature that is desirable, and the volume constraint remains active.

Table 2: Gray scale constraints for the arch problem

| Target δ (%) | 1.0 | 0.7 | 0.5 | 0.4 | 0.2 | 0.1 | Number of FEs |
|-----------------------|------|------|------|------|------|------|------------------|
| Achieved δ (%) | 1.34 | 0.96 | 0.89 | 0.81 | 0.64 | 0.54 | 100×50 |
| | 1.25 | 0.71 | 0.67 | 0.65 | 0.44 | 0.44 | 200×100 |

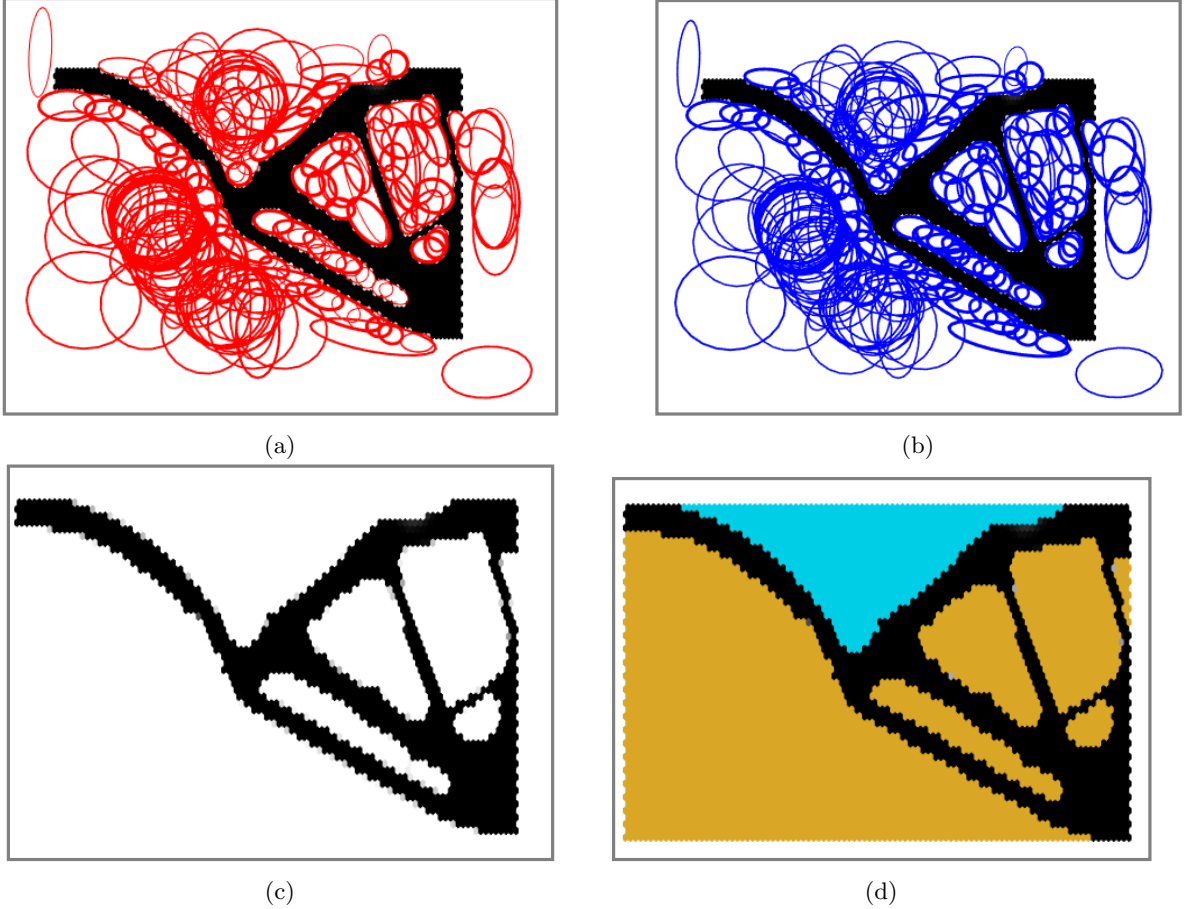


Figure 11: A symmetrical half optimized design for piston design after 400 MMA iterations (a) Optimized material layout with final elliptical masks whose line widths are proportional to their γ_j , (b) Material layout with final elliptical masks whose line widths are proportional to their α_j , (c) Optimized material layout with $GS_I = 0.78\%$ and (d) Optimized material layout with final pressure field.

5.2 Piston design

The pressure-loaded design for piston loadbearing structure was first presented in [30], which is taken herein as a second structure problem. The design domain specification with dimension $L_x \times L_y = 0.12 \times 0.04\text{m}^2$ is displayed in Fig. 6b. A vertical symmetry line exists for the design domain that is used herein to solve only a symmetrical part of the domain.

We use $N_{\text{ex}} \times N_{\text{ey}} = 100 \times 50$ hexagonal FEs and $N_{\text{mx}} \times N_{\text{my}} = 20 \times 10$ elliptical negative masks to

parametrize and determine the optimized material layout of the symmetrical design, respectively. Volume fraction and gray scale constraint are set to 0.25 and 0.001 respectively. The upper bound on α_j is set to 30. The maximum number of MMA iterations is set to 400. $S = 0.05$ is set for mask variable movement. We refer to Table 1 for other design parameters.

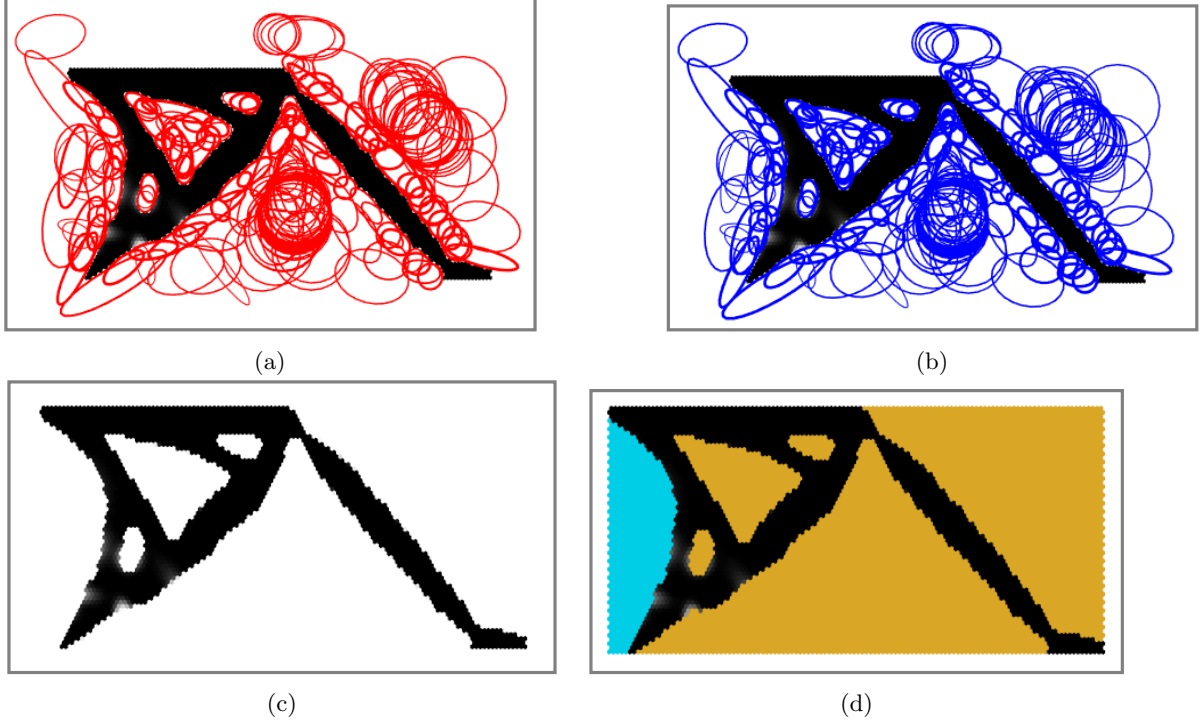


Figure 12: A symmetrical half optimized design for inverter mechanism after 600 MMA iterations (a) Optimized material layout with final elliptical masks whose line widths are proportional to their γ_j , (b) Material layout with final elliptical masks whose line widths are proportional to their α_j , (c) Optimized material layout with $GS_I = 1.37\%$ and (d) Optimized material layout with final pressure field.

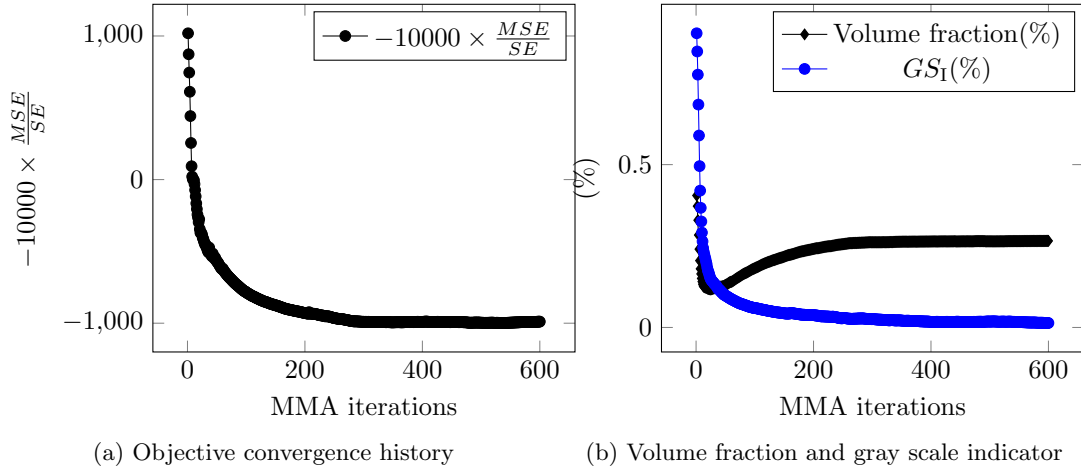


Figure 13: Objective and constraints convergence plots for the inverter mechanism.

A symmetrical half optimized piston design is displayed in Fig. 11. Plots with masks considering the values of γ_j and α_j proportion to the line widths of masks are depicted in Fig. 11a and 11b respectively. One notices that α_j and γ_j vary differently as noted in the arch problem result too. Specifically, nearly all masks whose boundaries define the contour of the continuum seem to have higher α_j , as expected, since this helps boundary FEs attain states close to the solid state. However, not all γ_j are high for the same masks. This suggests that selective dilation/erosion may be occurring at the continuum boundaries

in an attempt to satisfy the gray scale constraint. The optimized piston design resembles the previously obtained results for the same problem [2, 30]. The final normalized compliance, volume fraction and GS_I are 10.97 N m, 0.25 and 0.78%, respectively. The volume constraint is satisfied and active at the end of optimization, however gray scale constraint is close to though not quite satisfied. Reasons could be as mentioned in the Section 5.1.2. Next, we solve pressure-actuated compliant mechanisms.

5.3 Pressure-actuated CMs

Pressure-actuated inverter and Gripper CMs are designed using a multi-criterion objective (Eq. 19) with volume and gray scale indicator constraints.

The symmetric half designs for inverter and gripper mechanisms are depicted in Fig. 7a and 7b, respectively. $L_x \times L_y = 0.02 \times 0.01 \text{ m}^2$ is set for each mechanism. Figures also depict the output location and the direction of movement for each mechanism using red thick arrows. For the inverter mechanism, an inverse motion with respect to the pressure loading direction is sought, whereas a perpendicular gripping motion is desired in case of the gripper mechanism. To provide a proper seat for the workpiece, a void passive region having dimension $\frac{L_x}{5} \times \frac{L_y}{5}$ is provided and for gripping jaws (solid passive regions) dimension $\frac{L_x}{5} \times \frac{L_y}{40}$ are set. Springs with stiffness $k_s = 1 \times 10^5 \text{ N m}$ are attached at the output location of inverter and gripper mechanisms. These springs represent the workpiece stiffnesses at the output locations. $N_{ex} \times N_{ey} = 120 \times 60 \text{ FEs}$ are employed to describe the design domains. The number of elliptical masks is set to $N_{mx} \times N_{my} = 20 \times 10$ for both. Volume fraction for each mechanism is set to 0.30. δ for GS_I is chosen as 0.001. The maximum number MMA iterations is set to 600. The upper bounds on α_j and γ_j for the inverter mechanism used are 20, while for the gripper mechanisms those are 25 and 10, respectively. Step lengths (Eq. 30) for inverter and gripper are 0.01 and 0.025 respectively.

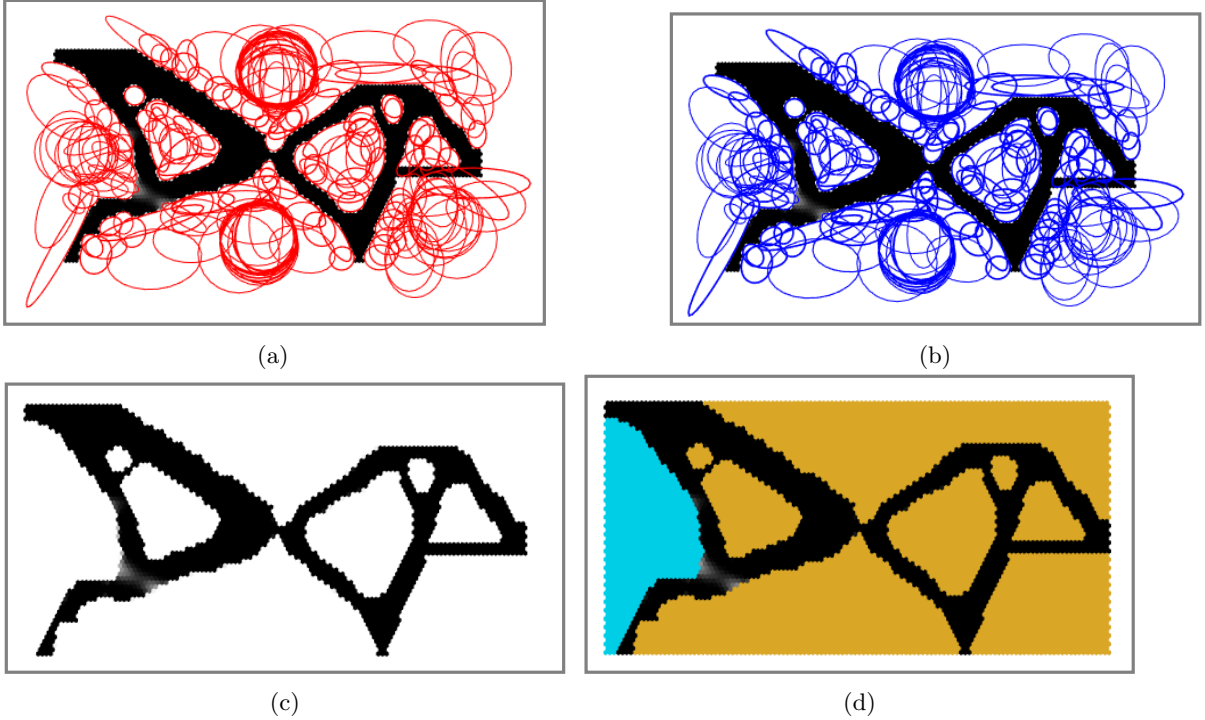


Figure 14: A symmetrical half optimized design for gripper mechanism after 600 MMA iterations (a) Optimized material layout with final elliptical masks whose line widths are proportional to their γ_j , (b) Material layout with final elliptical masks whose line widths are proportional to their α_j , (c) Optimized material layout with $GS_I = 0.81\%$, and (d) Optimized material layout with final pressure field.

The optimized designs for inverter and gripper mechanisms are depicted in Fig. 12 and 14 respectively. Masks with optimized CMs with γ_j and α_j represented by their line thickness are plotted in Fig. 12a, 14a and Fig. 12b, 14b, respectively. Fig. 12c and 14c show the optimized results with pressure field.



Figure 15: Deformed profiles for inverter and gripper mechanisms are displayed in (a) and (b) respectively. The actual deformation is magnified by 10 times for visibility purpose.

The final volume fraction for inverter and gripper mechanisms are 0.266 and 0.261, respectively and the final recorded gray scale indicator are 1.37% and 0.81% respectively. In both cases volume constraints are satisfied, however GS_I constraints do not satisfy. The optimized CMs with pressure field for the inverter and gripper mechanisms are depicted in Fig. 12d and 14d, respectively. One notes that to contain the pressure loads, the optimizer provides a chamber like inflated design at the input locations. The objective and constraints convergence plots for the optimized inverter mechanism are displayed in Fig. 13a and 13b respectively. At the end of the optimization process, these plots converge smoothly. The deformed profiles for the inverter and gripper mechanisms with their pressure field are illustrated in Fig. 15a and 15b respectively. The obtained motions of the output nodes of the mechanisms are as they are designed for.

6 Closure

The presented Material Mask Overlay Strategy (MMOS) topology optimization approach gives pressure-loaded structure and pressure-actuated compliant mechanism designs close to black and white. The final output displacements of these mechanisms are as expected. Negative elliptical masks are used, and for each mask, in addition to its position, size and orientation, logistic variable and exponent are posed as design variables. High value of the logistic variable leads to material addition near the mask boundary. In contrast, large value of the exponent results in material erosion inside and outside the boundary. By optimally determining their values for each mask, finite element densities can be controlled indirectly, leading to near black and white topologies, especially in presence of an explicit, gray scale constraint.

Hexagonal elements (honeycomb tessellation) are used to describe the design domains, which provide edge-connectivity and thus, point-connections and checkerboard patterns get automatically vanished from the optimized designs. To relate pressure field with the material density vector, Darcy's law with a drainage term is employed wherein the flow coefficient of each element is interpolated using a smooth Heaviside projection function. The formulation facilitates determining of pressure loading surfaces/curves implicitly as the topology optimization evolves wherein the span of pressure gradient alters with topology optimization iterations. The pressure field is then transformed into nodal forces using Wachspress shape functions employed to model hexagonal elements. The importance of drainage term with hexagonal elements is demonstrated using a design domain containing multiple solid finite elements layers.

The approach provides automatic and computationally inexpensive evaluation of the load sensitivity terms while determining objective sensitivities using the adjoint-variable method. The optimized pressure-actuated compliant mechanisms are designed with small deformation mechanics assumptions. Extending the approach for large deformation problems for soft (compliant) robotic designs will have additional challenges, e.g., treating the pressure loads as follower forces, and thus, it needs a dedicated and detailed investigation, which can be one of the interesting future directions. Extending the proposed methodology to three dimensions can be another prospective study.

Acknowledgments

P. Kumar acknowledges financial support from the Science & Engineering research board, Department of Science and Technology, Government of India under the project file number R/JF/2020/000023. The authors thank Prof. Krister Svanberg for providing MATLAB codes of the MMA optimizer.

Appendix

A Wachspress shape functions

A hexagonal element with vertices $V_i|_{i=1,2,3,\dots,6}$ in ξ co-ordinates system is depicted via Fig. 16. C_c is the circumscribing circle with radius 1 unit. One finds the coordinates of V_i as $\left((\xi_1^i, \xi_2^i) \equiv \left(\cos\left(\frac{(2i-1)\pi}{6}\right), \sin\left(\frac{(2i-1)\pi}{6}\right)\right)\right)$. Let N_i be the Wachspress shape function corresponding to node i , i.e., vertex V_i (Fig. 16). Using co-ordinate geometry, one writes the equations of straight lines l_i as

$$\left. \begin{aligned} l_1(\xi) &\equiv \xi_1 + \sqrt{3}\xi_2 - \sqrt{3} = 0 \\ l_2(\xi) &\equiv -\xi_1 + \sqrt{3}\xi_2 - \sqrt{3} = 0 \\ l_3(\xi) &\equiv 2\xi_1 + \sqrt{3} = 0 \\ l_4(\xi) &\equiv \xi_1 + \sqrt{3}\xi_2 + \sqrt{3} = 0 \\ l_5(\xi) &\equiv -\xi_1 + \sqrt{3}\xi_2 + \sqrt{3} = 0 \\ l_6(\xi) &\equiv 2\xi_1 - \sqrt{3} = 0 \end{aligned} \right\}, \quad (\text{A.1})$$

and likewise, one finds the equation of circle C_s (cf. Fig. 16, passing through P_{ii+2}) as

$$C_s(\xi) \equiv \xi_1^2 + \xi_2^2 - 3 = 0. \quad (\text{A.2})$$

Note that straight lines l_i and l_{i+2} intersect at point P_{ii+2} (Fig. 16). The shape function of node 1, i.e., N_1 is determined as [39]

$$N_1 = s_1 \frac{l_2(\xi)l_3(\xi)l_4(\xi)l_5(\xi)}{C_s(\xi)}, \quad (\text{A.3})$$

where s_1 , a constant, is extracted using the Kronecker-delta property of a shape function, which is defined as

$$N_i(\xi_j) = \delta_{ij} = \begin{cases} 1, & \text{if } i = j \\ 0, & \text{if } i \neq j \end{cases}. \quad (\text{A.4})$$

Now, in view of co-ordinates⁴ of node 1, i.e., (ξ_1^1, ξ_2^1) , Eqs. (A.3) and (A.4), one finds

$$s_1 = \frac{C_s(\xi_1^1, \xi_2^1)}{l_2(\xi_1^1, \xi_2^1)l_3(\xi_1^1, \xi_2^1)l_4(\xi_1^1, \xi_2^1)l_5(\xi_1^1, \xi_2^1)} = \frac{1}{18}. \quad (\text{A.5})$$

Likewise, one can find Wachspress shape functions corresponding to the remaining nodes, respective constants which can be summarized as

$$\left. \begin{aligned} N_1(\xi) &= \frac{(-\xi_1 + \sqrt{3}\xi_2 - \sqrt{3})(2\xi_1 + \sqrt{3})(\xi_1 + \sqrt{3}\xi_2 + \sqrt{3})(-\xi_1 + \sqrt{3}\xi_2 + \sqrt{3})}{18(\xi_1^2 + \xi_2^2 - 3)} \\ N_2(\xi) &= \frac{(2\xi_1 + \sqrt{3})(\xi_1 + \sqrt{3}\xi_2 + \sqrt{3})(-\xi_1 + \sqrt{3}\xi_2 + \sqrt{3})(2\xi_1 - \sqrt{3})}{18(\xi_1^2 + \xi_2^2 - 3)} \\ N_3(\xi) &= -\frac{(\xi_1 + \sqrt{3}\xi_2 + \sqrt{3})(-\xi_1 + \sqrt{3}\xi_2 + \sqrt{3})(2\xi_1 - \sqrt{3})(\xi_1 + \sqrt{3}\xi_2 - \sqrt{3})}{18(\xi_1^2 + \xi_2^2 - 3)} \\ N_4(\xi) &= \frac{(-\xi_1 + \sqrt{3}\xi_2 + \sqrt{3})(2\xi_1 - \sqrt{3})(\xi_1 + \sqrt{3}\xi_2 - \sqrt{3})(-\xi_1 + \sqrt{3}\xi_2 - \sqrt{3})}{18(\xi_1^2 + \xi_2^2 - 3)} \\ N_5(\xi) &= \frac{(2\xi_1 - \sqrt{3})(\xi_1 + \sqrt{3}\xi_2 - \sqrt{3})(-\xi_1 + \sqrt{3}\xi_2 - \sqrt{3})(2\xi_1 + \sqrt{3})}{18(\xi_1^2 + \xi_2^2 - 3)} \\ N_6(\xi) &= -\frac{(\xi_1 + \sqrt{3}\xi_2 - \sqrt{3})(-\xi_1 + \sqrt{3}\xi_2 - \sqrt{3})(2\xi_1 + \sqrt{3})(\xi_1 + \sqrt{3}\xi_2 + \sqrt{3})}{18(\xi_1^2 + \xi_2^2 - 3)} \end{aligned} \right\}. \quad (\text{A.6})$$

⁴ $\xi_1^1 = \cos(\frac{\pi}{6})$, $\xi_2^1 = \sin(\frac{\pi}{6})$

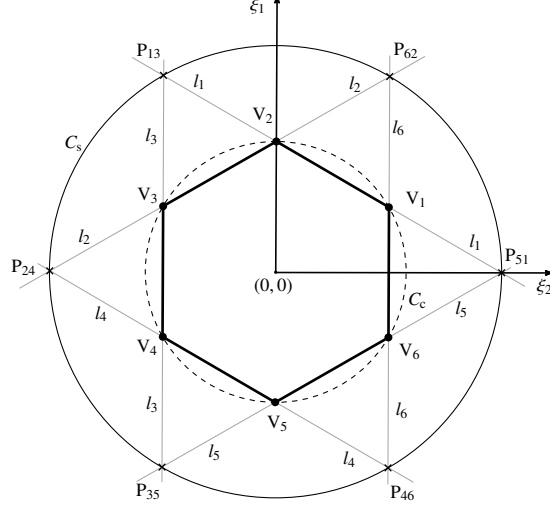


Figure 16: Definition of the shape functions for a regular hexagonal element with vertices $V_i |_{i=1,2,\dots,6}$ and circumscribing circle C_c with radius 1 unit. The co-ordinates the vertex V_i are $\left((\xi_1^i, \xi_2^i) \equiv \left(\cos\left(\frac{(2i-1)\pi}{6}\right), \sin\left(\frac{(2i-1)\pi}{6}\right)\right)\right)$. Straight lines l_i as depicted pass through vertices $V_i V_{i-1}$. Straight lines l_i and l_{i+2} intersect at point P_{i+2} . A circle C_s passing through points P_{i+2} is drawn, whose radius is equal to $\sqrt{3}$ units.

B Numerical quadrature points

Numerical quadrature rule is employed to find the integration pertaining to the finite element formulation for solving PDEs corresponding to fluid and mechanical balanced equations. As per [43], quadrature points for a hexagonal element are tabulated below (Table 3) and a function can be integrated as

$$\int_{\Omega_j} f dV \approx w_o f(0, 0) + \sum_{k=2}^{k_{\max}} \sum_{i=1}^6 w_k f\left(r_k, \alpha_k + i\frac{\pi}{3}\right). \quad (\text{B.1})$$

In Table 3, N is the number of integration points having co-ordinates $(\xi_1^a, \xi_2^a) = (r_k \cos(\alpha_k + \frac{i\pi}{3}), r_k \sin(\alpha_k + \frac{i\pi}{3}))$. $i = 1, 2, 3, \dots, 6$, if $k > 1$, and $i = 1$, if $k = 1$, corresponds to single integration point at center $(0, 0)$. For $k > 1$, six integration points lie on the a circle with center at $(0, 0)$ and radius r_k . w_k indicate the weights for these Gauss points. We have used $k = 2$, i.e, $N = 7$ quadrature points in this paper. Note that the quadrature rule is invariant under a rotation of 60° for a hexagonal FE [43].

Table 3: Quadrature points for a hexagonal element

| Cases | r_k | α_k | w_k |
|--------------------------------------|-------------------|-------------------|-------------------|
| 1, $k = 2$, $N = 1 + 6(k - 1) = 7$ | 0.0000 | 0.0000 | 0.255952380952381 |
| | 0.748331477354788 | 0.0000 | 0.124007936507936 |
| 2, $k = 3$, $N = 1 + 6(k - 1) = 13$ | 0.0000 | 0.0000 | 0.174588684325077 |
| | 0.657671808727194 | 0.0000 | 0.115855303626943 |
| | 0.943650632725263 | 0.523681372148045 | 0.021713248985544 |
| 3, $k = 4$, $N = 1 + 6(k - 1) = 19$ | 0.0000 | 0.0000 | 0.110826547228661 |
| | 0.792824967172091 | 0.0000 | 0.037749166510143 |
| | 0.537790663359878 | 0.523598775598299 | 0.082419705350590 |
| | 0.883544457934942 | 0.523598775598299 | 0.028026703601157 |
| 4, $k = 5$, $N = 1 + 6(k - 1) = 25$ | 0.0000 | 0.0000 | 0.087005549094808 |
| | 0.487786213872069 | 0.0000 | 0.071957468118574 |
| | 0.820741657108524 | 0.0000 | 0.027500185650866 |
| | 0.771806696813652 | 0.523598775598299 | 0.045248932131663 |
| | 0.957912268790000 | 0.523598775598299 | 0.007459892497607 |

References

- [1] V. B. Hammer and N. Olhoff, “Topology optimization of continuum structures subjected to pressure loading,” *Structural and Multidisciplinary Optimization*, vol. 19, no. 2, pp. 85–92, 2000.
- [2] P. Kumar, J. Frouws, and M. Langelaar, “Topology optimization of fluidic pressure-loaded structures and compliant mechanisms using the darcy method,” *Structural and Multidisciplinary Optimization*, vol. 61, pp. 1637–1655, 2020.
- [3] O. Sigmund and K. Maute, “Topology optimization approaches,” *Structural and Multidisciplinary Optimization*, vol. 48, no. 6, pp. 1031–1055, 2013.
- [4] A. Saxena, “A material-mask overlay strategy for continuum topology optimization of compliant mechanisms using honeycomb discretization,” *Journal of Mechanical Design*, vol. 130, p. 082304, 2008.
- [5] R. Saxena and A. Saxena, “On honeycomb representation and sigmoid material assignment in optimal topology synthesis of compliant mechanisms,” *Finite Elements in Analysis and Design*, vol. 43, no. 14, pp. 1082–1098, 2007.
- [6] M. Langelaar, “The use of convex uniform honeycomb tessellations in structural topology optimization,” in *7th world congress on structural and multidisciplinary optimization, Seoul, South Korea, May*, pp. 21–25, 2007.
- [7] C. Talischi, G. H. Paulino, and C. H. Le, “Honeycomb wachspress finite elements for structural topology optimization,” *Structural and Multidisciplinary Optimization*, vol. 37, no. 6, pp. 569–583, 2009.
- [8] A. Saxena, “Topology design with negative masks using gradient search,” *Structural and Multidisciplinary Optimization*, vol. 44, no. 5, pp. 629–649, 2011.

- [9] P. Kumar and A. Saxena, “On topology optimization with embedded boundary resolution and smoothing,” *Structural and Multidisciplinary Optimization*, vol. 52, no. 6, pp. 1135–1159, 2015.
- [10] A. Saxena, “Are circular shaped masks adequate in adaptive mask overlay topology synthesis method?,” *Journal of Mechanical Design*, vol. 133, no. 1, p. 011001, 2011.
- [11] P. Kumar, *Synthesis of Large Deformable Contact-Aided Compliant Mechanisms Using Hexagonal Cells and Negative Circular Masks*. PhD dissertation, Indian Institute of Technology Kanpur, India, 2017.
- [12] J. A. Norato, “Topology optimization with supershapes,” *Structural and Multidisciplinary Optimization*, vol. 58, no. 2, pp. 415–434, 2018.
- [13] N. Singh, P. Kumar, and A. Saxena, “On topology optimization with elliptical masks and honeycomb tessellation with explicit length scale constraints,” *Structural and Multidisciplinary Optimization*, vol. 62, no. 3, pp. 1227–1251, 2020.
- [14] X. Guo, W. Zhang, and W. Zhong, “Doing topology optimization explicitly and geometrically—a new moving morphable components based framework,” *Journal of Applied Mechanics*, vol. 81, no. 8, 2014.
- [15] P. Kumar, P. Fanzio, L. Sasso, and M. Langelaar, “Compliant fluidic control structures: Concept and synthesis approach,” *Computers & Structures*, vol. 216, pp. 26–39, 2019.
- [16] B. Zhu, X. Zhang, H. Zhang, J. Liang, H. Zang, H. Li, and R. Wang, “Design of compliant mechanisms using continuum topology optimization: a review,” *Mechanism and Machine Theory*, vol. 143, p. 103622, 2020.
- [17] P. Kumar, C. Schmidleithner, N. Larsen, and O. Sigmund, “Topology optimization and 3D printing of large deformation compliant mechanisms for straining biological tissues,” *Structural and Multidisciplinary Optimization*, vol. 63, no. 3, pp. 1351–1366, 2021.
- [18] A. Saxena and G. K. Ananthasuresh, “On an optimal property of compliant topologies,” *Structural and multidisciplinary optimization*, vol. 19, no. 1, pp. 36–49, 2000.
- [19] J. Du and N. Olhoff, “Topological optimization of continuum structures with design-dependent surface loading—part I: new computational approach for 2D problems,” *Structural and Multidisciplinary Optimization*, vol. 27, no. 3, pp. 151–165, 2004.
- [20] M. B. Fuchs and N. N. Y. Shemesh, “Density-based topological design of structures subjected to water pressure using a parametric loading surface,” *Structural and Multidisciplinary Optimization*, vol. 28, no. 1, pp. 11–19, 2004.
- [21] H. Zhang, X. Zhang, and S. Liu, “A new boundary search scheme for topology optimization of continuum structures with design-dependent loads,” *Structural and Multidisciplinary Optimization*, vol. 37, no. 2, pp. 121–129, 2008.
- [22] E. Lee and J. R. Martins, “Structural topology optimization with design-dependent pressure loads,” *Computer Methods in Applied Mechanics and Engineering*, vol. 233, pp. 40–48, 2012.
- [23] Z.-m. Li, J. Yu, Y. Yu, and L. Xu, “Topology optimization of pressure structures based on regional contour tracking technology,” *Structural and Multidisciplinary Optimization*, vol. 58, no. 2, pp. 687–700, 2018.
- [24] O. Ibbadode, Z. Zhang, P. Rahnama, A. Bonakdar, and E. Toyserkani, “Topology optimization of structures under design-dependent pressure loads by a boundary identification-load evolution (BILE) model,” *Structural and Multidisciplinary Optimization*, vol. 62, pp. 1865–1883, 2020.
- [25] Q. Xia, M. Y. Wang, and T. Shi, “Topology optimization with pressure load through a level set method,” *Computer Methods in Applied Mechanics and Engineering*, vol. 283, pp. 177–195, 2015.
- [26] C. Wang, M. Zhao, and T. Ge, “Structural topology optimization with design-dependent pressure loads,” *Structural and Multidisciplinary Optimization*, vol. 53, no. 5, pp. 1005–1018, 2016.

- [27] R. Picelli, A. Neofytou, and H. A. Kim, “Topology optimization for design-dependent hydrostatic pressure loading via the level-set method,” *Structural and Multidisciplinary Optimization*, vol. 60, no. 4, pp. 1313–1326, 2019.
- [28] B. C. Chen and N. Kikuchi, “Topology optimization with design-dependent loads,” *Finite elements in analysis and design*, vol. 37, no. 1, pp. 57–70, 2001.
- [29] B. C. Chen, E. C. Silva, and N. Kikuchi, “Advances in computational design and optimization with application to mems,” *International Journal for Numerical Methods in Engineering*, vol. 52, no. 1-2, pp. 23–62, 2001.
- [30] B. Bourdin and A. Chambolle, “Design-dependent loads in topology optimization,” *ESAIM: Control, Optimisation and Calculus of Variations*, vol. 9, pp. 19–48, 2003.
- [31] O. Sigmund and P. M. Clausen, “Topology optimization using a mixed formulation: An alternative way to solve pressure load problems,” *Computer Methods in Applied Mechanics and Engineering*, vol. 196, no. 13-16, pp. 1874–1889, 2007.
- [32] O. C. Zienkiewicz and R. L. Taylor, *The Finite Element Method for Solid and Structural Mechanics*. Butterworth-heinemann, 2005.
- [33] B. Zheng, C. J. Chang, and H. C. Gea, “Topology optimization with design-dependent pressure loading,” *Structural and Multidisciplinary Optimization*, vol. 38, no. 6, pp. 535–543, 2009.
- [34] S. Vasista and L. Tong, “Design and testing of pressurized cellular planar morphing structures,” *AIAA journal*, vol. 50, no. 6, pp. 1328–1338, 2012.
- [35] H. Panganiban, G. W. Jang, and T. J. Chung, “Topology optimization of pressure-actuated compliant mechanisms,” *Finite Elements in Analysis and Design*, vol. 46, no. 3, pp. 238–246, 2010.
- [36] E. M. de Souza and E. C. N. Silva, “Topology optimization applied to the design of actuators driven by pressure loads,” *Structural and Multidisciplinary Optimization*, vol. 61, no. 5, pp. 1763–1786, 2020.
- [37] P. Kumar, R. A. Sauer, and A. Saxena, “Synthesis of C^0 path-generating contact-aided compliant mechanisms using the material mask overlay method,” *Journal of Mechanical Design*, vol. 138, no. 6, p. 062301, 2016.
- [38] P. Kumar, A. Saxena, and R. A. Sauer, “Computational synthesis of large deformation compliant mechanisms undergoing self and mutual contact,” *Journal of Mechanical Design*, vol. 141, no. 1, p. 012302, 2019.
- [39] E. L. Wachspress, “A rational finite element basis.,” 1975.
- [40] P. Kumar and M. Langelaar, “On topology optimization of design-dependent pressure-loaded three-dimensional structures and compliant mechanisms,” *International Journal for Numerical Methods in Engineering*, vol. 122, no. 9, pp. 2205–2220, 2021.
- [41] O. Sigmund, “Morphology-based black and white filters for topology optimization,” *Structural and Multidisciplinary Optimization*, vol. 33, no. 4-5, pp. 401–424, 2007.
- [42] K. Svanberg, “The method of moving asymptotes—a new method for structural optimization,” *International journal for numerical methods in engineering*, vol. 24, no. 2, pp. 359–373, 1987.
- [43] J. Lyness and G. Monegato, “Quadrature rules for regions having regular hexagonal symmetry,” *SIAM Journal on Numerical Analysis*, vol. 14, no. 2, pp. 283–295, 1977.